

Topological mechanics of origami and kirigami

Bryan Gin-ge Chen,¹ Bin Liu,² Arthur A. Evans,³ Jayson Paulose,¹ Itai Cohen,² Vincenzo Vitelli,¹ and C.D. Santangelo³

¹*Instituut-Lorentz, Universiteit Leiden, 2300 RA Leiden, The Netherlands*

²*Department of Physics, Cornell University, NY 14853, USA*

³*Department of Physics, University of Massachusetts, Amherst, MA 01002, USA*
(Dated: October 14, 2018)

Origami and kirigami have emerged as potential tools for the design of mechanical metamaterials whose properties such as curvature, Poisson's ratio, and existence of metastable states can be tuned using purely geometric criteria. A major obstacle to exploiting this property is the scarcity of tools to identify and program the flexibility of fold patterns. We exploit a recent connection between spring networks and quantum topological states to design origami with localized folding motions at boundaries and study them both experimentally and theoretically. These folding motions exist due to an underlying topological invariant rather than a local imbalance between constraints and degrees of freedom. We give a simple example of a quasi-one dimensional folding pattern that realizes such topological states. We also demonstrate how to generalize these topological design principles to two dimensions. A striking consequence is that a domain wall between two topologically distinct, mechanically rigid structures is deformable even when constraints locally match the degrees of freedom.

Recent interest in origami mechanisms has been spurred by advances in fabrication and manufacturing [1–3], as well as a realization that folded structures can form the basis of mechanical metamaterials [4–8]. The ability to identify kinematic mechanisms – allowable folding motions of a crease pattern – is critical to the use of origami to design new deployable structures and mechanical metamaterials. For example, the mechanism in the celebrated Miura ori that allows it to furl and unfurl in a single motion [9, 10] is also the primary determinant of the fold pattern's negative Poisson ratio [4, 5]. Identifying these mechanisms becomes more challenging when the number of apparent constraints matches the number of degrees of freedom (DOF).

We show that periodically-folded sheets may exhibit distinct mechanical “phases” characterized by a topological invariant called the *topological polarization*, recently introduced by Kane and Lubensky [11] using a mapping of mechanically marginal structures to topological insulators [12]. The importance of this invariant has emerged in the study of linkages [13], the soft modes of spring networks [14] and buckling [15]. As in these examples, the phases exhibit localized vibrational modes on the boundary, and transitions from one topological polarization to another are characterized by the appearance of bulk modes that cost zero energy. These are the hallmarks of topologically protected behaviour in classical mechanical systems [16–23]. Topology provides a new knob to tune how materials and, as we show here, origami and kirigami structures, respond to external perturbations.

To demonstrate the power of this approach, we introduce an example of a one-dimensional strip of origami analogous to the Su-Schrieffer-Heeger polyacetylene model [11]. It admits localized modes and stresses protected by topology, which we realize and characterize in experiments. Additionally we show how to generalize this to two-dimensionally periodic origami sheets,

where we have observed a striking property that causes origami without holes to have zero topological polarization. We give examples of hinged structures with holes (kirigami) that do admit distinct polarizations and thus can be used as building blocks for metasheets with programmable softness and stiffness.

We denote by *origami*, mechanical structures consisting of rigid flat polygonal plates joined by hinges. We will first discuss origami with no missing plates or “holes”, and then generalize to *kirigami*, defined to be origami where such holes are allowed. We will consider the mechanics of origami in the geometrical limit – folds will cost zero energy and faces do not stretch or bend.

When there is an exact balance between DOF and constraints in a periodic structure, the structure is marginally rigid [24, 25]. In such a case, new mechanical properties emerge due to the close connection between the number of soft modes and the presence of boundaries or defects [26]. Solids with marginal rigidity exhibit large, often nonlinear, response to small mechanical perturbations [27–29]. A recent realization is that the flexibility of such solids may be influenced by *nontrivial topology* in the phonon band structure [11, 14]. Here, we show how to extend these topological ideas to origami and kirigami. We start with a simple quasi-one dimensional origami structure.

Consider an origami strip of zig-zagging rigid quadrilateral plates, depicted in Fig. 1, consisting of a periodically-repeating unit cell of two four-fold vertices. Each vertex in a cell (labeled by $n = 1, 2$) has four creases (Fig. 1(a)), and one DOF [30] that we track with the dihedral angles of the bolded crease, $f_n(j)$, where j indexes the unit cell (Fig. 1(b)). Each adjacent pair of dihedral angles is coupled by the kinematics of the intervening vertex. As each vertex contributes a DOF and a constraint, this origami structure has marginal rigidity.

The mechanical response of the origami strip can be

analyzed since its configurations may be determined analytically as functions of the fold pattern angles $\beta_1, \beta_2, \gamma_1$ and γ_2 (defined in Fig. 1(a)). We define a generalized displacement $u(j) = \cos f_2(j) + 1$. The function $u(j)$ encodes the dihedral angle f_2 of the right-most fold of unit cell j , and satisfies

$$u(j+1) = \kappa(\alpha, \beta_1, \beta_2, \gamma_1, \gamma_2)u(j), \quad (1)$$

where

$$\kappa = \left[\frac{\sin(\alpha - \beta_1) \sin(\alpha - \gamma_1)}{\sin(\alpha + \beta_1) \sin(\alpha + \gamma_1)} \right] \left[\frac{\sin(\alpha - \beta_2) \sin(\alpha - \gamma_2)}{\sin(\alpha + \beta_2) \sin(\alpha + \gamma_2)} \right]. \quad (2)$$

The derivation is an application of the spherical law of cosines and is given in the SI. The fact that $u(j)$ determines $u(j+1)$ implies that the strip has one global degree of freedom. Eq. (1) is solved by an exponential function $u(j) = u(0) \exp[j \ln(\kappa)]$ with deformation localized to one side or the other, according to the sign of the inverse decay length $l^{-1} = \ln \kappa$.

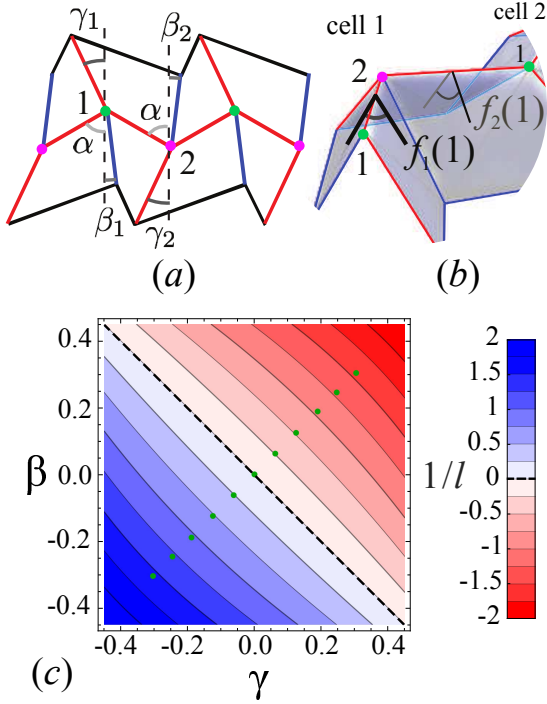


FIG. 1: A quasi-one-dimensional origami strip. (a) A unit cell of the fold pattern corresponding to the origami mechanism with planar angles labeled. Red (blue) creases are mountain (valley) folds, respectively. (b) A 3D depiction of a part of the strip with folding angles $f_i(n)$ labeled. (c) The phase diagram for the fold pattern for $\alpha = \pi/3$, $\beta \equiv \beta_1 = \beta_2$ and $\gamma \equiv \gamma_1 = \gamma_2$. The blue region is right-localized while the red region is left-localized; the contours and intensity of color follow $1/l$ (see legend). Configurations where folds at a vertex become collinear lie on $\gamma = \beta$, and the green points along that line were constructed in experiment (along this line, (γ, β) and $(-\gamma, -\beta)$ are related by a rotation in 3D).

A special role is played by fold patterns with $\kappa = 1$, where the decay length diverges and $u(j)$ neither grows nor shrinks. This is precisely the condition for which a global kinematic mechanism exists and the fold pattern is *deployable* [31]. The mechanical “phase diagram” in Fig. 1(c) shows the values of κ for patterns with $\gamma_1 = \gamma_2 \equiv \gamma, \beta_1 = \beta_2 \equiv \beta$. Deployable structures exist precisely on the dashed line separating the “phases” characterized by the sign of κ . This special state is realized by a row of the Miura ori fold pattern. More generically, however, as long as the sign of $\ln \kappa$ never changes, the deformation, $u(j)$, is localized even if the values of $\alpha, \beta_j, \gamma_j$ vary due to disorder or imperfections. The existence of phases of robust, boundary-localized zero-energy deformations separated by critical configurations with bulk zero modes is a signal that the origami strip has *topologically protected properties*.

To make the topology explicit, we calculate an invariant that characterizes the distinct topological phases of the marginally rigid origami strip. Unlike in periodic spring networks with marginal rigidity [11, 32, 33], a linear analysis is inadequate to capture the topology of the origami strip. Coplanar hinges in the flat state are redundant constraints, and this results in extra zero modes at linear order which do not extend to higher order. In the SI, we derive a rigidity matrix capturing the *second-order* deformations of this structure and show that it has the same pattern of entries as the Hamiltonian of the Su-Schrieffer-Heeger chain of Refs. 11, 34. Therefore, phases of the origami strip are characterized by their topological polarization [11], defined as a winding number of the determinant of the rigidity matrix. Indeed, the sign of $\ln \kappa$ is precisely correlated with the topological polarization. Structures for which $\kappa = 1$ (dashed line in Fig. 1(c)), for which the polarization is ill-defined, mark the transition between the two distinct topological phases.

To test the consequences of Eq. (1) away from the ideal limit, in a structure where faces can bend and hinges can twist, a mylar sheet (200 μm thick) is perforated by a laser cutter into the desired crease pattern, rendering it foldable along lines of perforations. We strengthen the facets by sandwiching the mylar sheet between pairs of 1 mm thick, plastic plates made of polylactic acid (PLA) on a 3D printer. To mount the plastic plates onto the mylar sheet, we use a pushed-in clip design: one facet has clips and the corresponding facet has holes. Equivalent holes are cut on the mylar sheet so that the clips can be pushed through to meet the holes on the plate on the other side of the mylar. An example of the assembled origami structure is shown in Fig. 2(a). Here, we fixed the angle $\alpha = \pi/3$ and set $\gamma \equiv \beta_1 = \gamma_1 = \beta_2 = \gamma_2$.

A video camera captured the deformation of the strip from above as it was symmetrically compressed. The position of each vertex was obtained via image analysis, and fit with a 3D model to reconstruct the complete morphology of the origami strip, as shown in Fig. 2(b). Finally, the folding angles along the interior creases were extracted from the 3D shape, and were used to compute

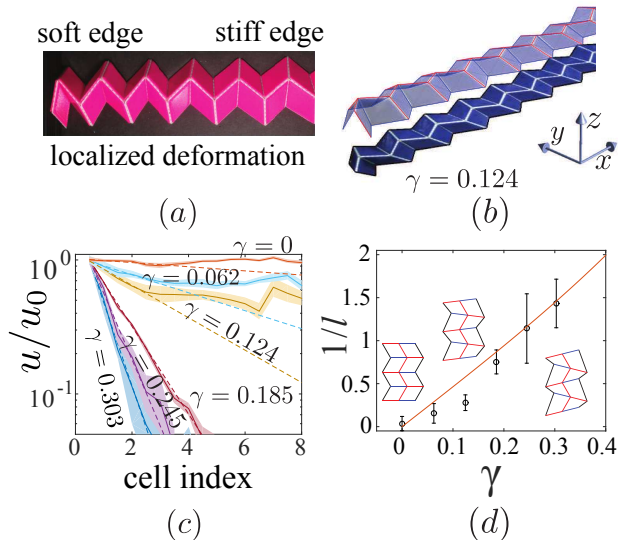


FIG. 2: (a) An image of the localized topological deformation in an experimental realization of the origami strip ($\alpha = \pi/3, \gamma_1 = \gamma_2 = \beta_1 = \beta_2 = 0.062$). (b) 3D reconstruction of the configuration of the strip from a flat image ($\gamma = 0.124$). (c) Normalized generalized strain u/u_0 as a function of distance from the deformable boundary (measured in number of vertices) from experiments (shaded curves) with fits to an exponential decay function (dashed lines). Folding angles $f_2(1)$ (related to u_0 via $u_0 = 1 + \cos f_2(1)$) at cell 1 varied from 1.06 to 1.45. (d) Decay lengths obtained from fits to the strain curves in (c) compared to analytical results for $l^{-1} = \ln \kappa$ (Eq. 2). The deviations for small γ are associated with an energetically costly “uniform bending mode” which requires facet deformation.

the generalized strain u . Fig. 2(c) shows the strain as a function of distance along the strip for samples with different values of the pattern parameter γ .

As shown by a semi-log fit (dashed lines in Fig. 2(c)), the strains decay exponentially at small distances from the highly-folded end. For small γ , the folding angles level off to a roughly constant value at larger distances, which violates Eq. (1). This saturation reflects a deviation from the ideal geometrical limit due to the finite flexibility of the facets and the finite crease thicknesses. Despite the non-ideality of the experimental origami strip, the decay lengths extracted from the fit are in good agreement with $1/l = \ln \kappa$ (Fig. 2(d)), highlighting the robustness of our topological design principle.

Having established that marginally rigid 1D periodic origami can exhibit topological phases, we now ask whether marginality also leads to similar phases in 2D origami. We first characterize the class of *marginally rigid* 2D periodic origami and show that they must have a triangulated crease pattern. To avoid trigonometric complexity inherent to a folding angle representation, we model the kinematics of triangulated origami as a central-force spring network with vertices as joints and hinges

as springs. Triangles in such a network automatically enforce the no-bending constraint on the facets. Arbitrary origami can be modeled with spring networks, but nontriangular faces require additional internal springs to remain rigid.

In this framework, each joint has 3 degrees of freedom and each spring adds one constraint, so marginal structures satisfy $E = 3V$ where E is the number of bonds and V is the number of joints. In a triangulated surface without a boundary, each of the F faces is a triangle, so $3F = 2E$. The Euler characteristic χ is defined as $\chi = V - E + F$; thus we obtain

$$E = 3(V - \chi). \quad (3)$$

Periodic origami structures in 2D have the topology of the torus and thus $\chi = 0$, which shows that *triangulations are marginally rigid*.

While achieving marginality in granular packings and glassy networks requires some fine-tuning in pressure or coordination, the analogous origami triangulations arise naturally. Any non-triangular plate in an origami pattern can be triangulated by adding diagonals, and the bending of non-triangular plates in real origami can be modeled as the addition of new creases [4, 6].

Since marginal rigidity arises naturally in periodic 2D triangulated structures, one might then expect a variety of topological phases by analogy with the 1D strip. Surprisingly, our calculations indicate otherwise. As discussed above, an analysis of the rigidity of *flat* origami must go beyond linear order. To bypass this complication, we consider periodic triangulated origami where we break the flat-state symmetry by introducing small vertical displacements to the vertices. The linear rigidity and topological properties of such a triangulated origami can be expressed directly in terms of the (Fourier-transformed) rigidity matrix \mathbf{R} for its associated spring network [11]. However, for all periodic fold patterns we have considered, the function $\det \mathbf{R}(\mathbf{q})$, *a priori* a complex-valued function, is in fact real-valued for all \mathbf{q} in the Brillouin zone [37]. Though a proof of this statement for all triangulated origami eludes us, extensive numerical tests of a large number of distinct fold patterns bear out this conjecture. We give details and partial results in the SI.

A consequence of the “reality” property is that the winding numbers of $\det \mathbf{R}(\mathbf{q})$ along any closed curves in the Brillouin zone (when defined) must be zero, and hence the topological polarization must vanish. Thus the localized boundary modes for such an origami must be isotropically distributed. Even if the hinges in a unit cell break left-right symmetry, the number of boundary modes on each edge of a finite patch is left-right and up-down symmetric. If, as we believe, all triangulated periodic origami structures have this property, the only way to get an imbalance in the number of zero modes at the boundary of origami is by locally removing constraints. This behavior contrasts with the 1D strips of origami as well as marginal spring networks confined to

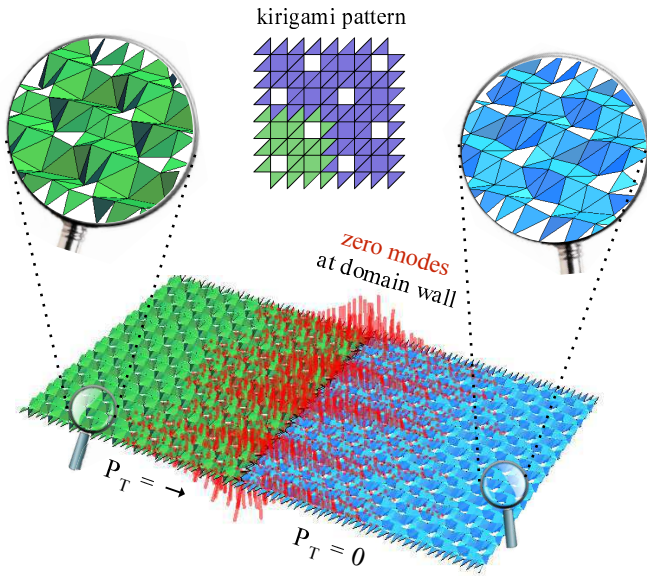


FIG. 3: An image of a topologically protected zero mode (red) at a domain wall between the two unit cells (left green with $\vec{P}_T = (1, 0)$ / right blue with $\vec{P}_T = (0, 0)$). Numerically the mode depicted has energy nearly indistinguishable from the translation modes. This is a close-up of a larger periodic system consisting of 50 unit cells by 5 unit cells, which is divided into two domains each of size 25 by 5 (two copies in the shorter direction are shown). The magnifying glass insets show the fine structure of four unit cells, and in between them is a schematic showing how the alternating quadrilateral plates, strips of triangles, and quadrilateral holes are joined by hinges. The actual unit cells are perturbed from this 2D pattern into 3D. Four unit cells are shown in the schematic, with one in the lower left highlighted in green.

2D and 3D periodic networks.

To find 2D periodic structures with a topological polarization, we consider the broader class of *kirigami*, structures with holes. Cutting out an adjacent pair of triangles removes one bond from the associated spring network, eliminating a constraint which can be compensated by merging a pair of triangles into a quadrilateral plate elsewhere in the unit cell. This process of cutting and merging preserves marginality, yet breaks the hidden symmetry and enables $\det \mathbf{R}(\mathbf{q})$ to be complex-valued. This procedure opens up the possibility of nonzero winding numbers of $\det \mathbf{R}(\mathbf{q})$ when the Brillouin zone is traversed.

As an example of the power of topological phases of kirigami in mechanical design, in Fig. 3, we show a do-

main wall separating two systems with different topological polarizations and a localized zero mode associated to that domain wall. Both kirigami structures have the same combinatorial graph underlying their plates and hinges (essentially a triangular network with two quadrilateral plates and two quadrilateral holes per unit cell), though they have different geometrical realizations. Details of the design of these structures are discussed in the SI. The zero mode renders the structure foldable in the vicinity of the domain wall, while it remains rigid further away. By contrast, a domain wall between kirigami patterns with the same polarization has no such localized modes, and the structure cannot be folded without stretching the plates (see SI). In general, domain walls between structures with different polarizations localize either zero modes, creating “soft” lines along which the system easily deforms, or “stressed” lines along which the system first bears loads under applied strains [15]. Similar effects may arise at point defects in otherwise uniform polarized structures [35].

We have demonstrated that origami and kirigami structures are characterized by a topological polarization. This topological polarization tells us that there are multiple ways for a fold pattern to be rigid; in the space of fold patterns, the topology tells us that those with different polarizations must be separated by globally flexible, i.e. deployable, realizations. Thus one can also exploit polarized origami and kirigami (necessarily rigid, by definition) to find deployable patterns. While topological modes in 1D linkages have been found to lead to propagating domain walls [13, 36], this is not possible for the 1D strip. In Eq. (2), κ depends only on the angles in the fold pattern, *not* the dihedral angles – this means that the topological polarization of the unit cell cannot change under physical deformations, which would be necessary for propagation. More broadly, the marginality that these topological invariants rely on is a generic feature of origami that is responsible for the rich connections between their geometry, topology and mechanics. Our results give strong constraints on the types of boundary modes that can be created in origami and will guide the design of fold patterns that achieve a desired, targeted mechanical response.

We acknowledge conversations with T.C. Lubensky and R.D. Kamien. We are grateful for funding from the NSF through EFRI ODISSEI-1240441 (AAE, BL, IC, CS). We acknowledge financial support from FOM (BGC, JP), from the D-ITP consortium (JP) and a VIDI grant (VV) funded by NWO.

[1] J. Ryu, M. D’Amato, X. Cui, K. N. Long, H. J. Qi, and M. L. Dunn, *Applied Physics Letters* **100**, 161908 (2012).
[2] M. T. Tolley, S. M. Felton, S. Miyashita, D. Aukes, D. Rus, and R. J. Wood, *Smart Materials and Structures* **23**, 094006 (2014).

[3] Y. Liu, M. Miskiewicz, M. J. Escuti, J. Genzer, and M. D. Dickey, *Journal of Applied Physics* **115**, 204911 (2014).
[4] Z. Y. Wei, Z. V. Guo, L. Dudte, H. Y. Liang, and L. Mahadevan, *Phys. Rev. Lett.* **110**, 215501 (2013).
[5] M. Schenk and S. D. Guest, *Proceedings of the National*

- Academy of Sciences **110**, 3276 (2013).
- [6] J. L. Silverberg, A. A. Evans, L. McLeod, R. C. Hayward, T. Hull, C. D. Santangelo, and I. Cohen, *Science* **345**, 647 (2014).
 - [7] C. Lv, D. Krishnaraju, G. Konjevod, H. Yu, and H. Jiang, *Scientific reports* **4** (2014).
 - [8] S. Waitukaitis, R. Menaut, B. G.-g. Chen, and M. van Hecke, *Phys. Rev. Lett.* **114**, 055503 (2015).
 - [9] K. Miura, *Proc. 31st Congr. Int. Astronaut. Federation IAF-8 0-A* **31**, 1 (1980).
 - [10] A. Evans, J. Silverberg, and C. Santangelo, *Phys. Rev. E* **92**, 013205 (2015).
 - [11] C. Kane and T. Lubensky, *Nature Physics* (2013).
 - [12] M. Z. Hasan and C. L. Kane, *Reviews of Modern Physics* **82**, 3045 (2010).
 - [13] B. G.-g. Chen, N. Upadhyaya, and V. Vitelli, *Proceedings of the National Academy of Sciences* **111**, 13004 (2014).
 - [14] T. Lubensky, C. Kane, X. Mao, A. Souslov, and K. Sun, *Reports on Progress in Physics* **78**, 073901 (2015).
 - [15] J. Paulose, A. S. Meussen, and V. Vitelli, *Proceedings of the National Academy of Sciences* **112**, 7639 (2015).
 - [16] E. Prodan and C. Prodan, *Physical Review Letters* **103**, 248101 (2009).
 - [17] H. C. Po, Y. Bahri, and A. Vishwanath (2014), 1410.1320.
 - [18] M. Xiao, G. Ma, Z. Yang, P. Sheng, Z. Q. Zhang, and C. T. Chan, *Nature Physics* **11** (2015).
 - [19] Z. Yang, F. Gao, X. Shi, X. Lin, Z. Gao, Y. Chong, and B. Zhang, *Physical Review Letters* **114**, 1 (2015).
 - [20] L. M. Nash, D. Kleckner, V. Vitelli, A. M. Turner, and W. T. M. Irvine, *Arxiv* (2015), 1504.03362v1.
 - [21] P. Wang, L. Lu, and K. Bertoldi, *Arxiv* (2015), 1504.01374v1.
 - [22] Y.-T. Wang, P.-G. Luan, and S. Zhang, *New Journal of Physics* **17**, 073031 (2015).
 - [23] R. Susstrunk and S. D. Huber, *Science* **349**, 47 (2015), 1503.06808v1.
 - [24] C. S. O’Hern, L. E. Silbert, A. J. Liu, and S. R. Nagel, *Phys. Rev. E* **68**, 011306 (2003).
 - [25] S. Alexander, *Phys. Rep.* **296**, 65 (1998).
 - [26] M. Wyart, S. Nagel, and T. Witten, *Europhysics Letters* **72**, 486 (2005).
 - [27] M. Wyart, H. Liang, A. Kabla, and L. Mahadevan, *Phys. Rev. Lett.* **101**, 215501 (2008).
 - [28] L. Gómez, A. Turner, M. van Hecke, and V. Vitelli, *Phys. Rev. Lett.* **108**, 058001 (2012).
 - [29] S. Ulrich, N. Upadhyaya, B. van Opheusden, and V. Vitelli, *Proceedings of the National Academy of Sciences* **110**, 20929 (2013).
 - [30] T. Hull, *Project origami: activities for exploring mathematics* (CRC Press, 2012).
 - [31] S. Pellegrino, *Deployable Structures* (Springer-Verlag Wien, 2001).
 - [32] L. Asimow and B. Roth, *Trans. Amer. Math. Soc.* **245**, 279 (1978).
 - [33] C. Calladine, *Int. J. Solids Struct.* **14**, 161 (1978).
 - [34] W. Su, J. Schrieffer, and A. Heeger, *Phys. Rev. Lett.* **42**, 1698 (1979).
 - [35] J. Paulose, B. G.-g. Chen, and V. Vitelli, *Nature Physics* **11**, 153 (2015).
 - [36] V. Vitelli, B. G.-g. Chen, and N. Upadhyaya, *arXiv preprint arXiv:1407.2890* (2015).
 - [37] More precisely, since the function $\det \mathbf{R}(\mathbf{q})$ is gauge dependent, the claim is that this is true in the gauge arising

from a “balanced” unit cell as defined in Ref. [11].

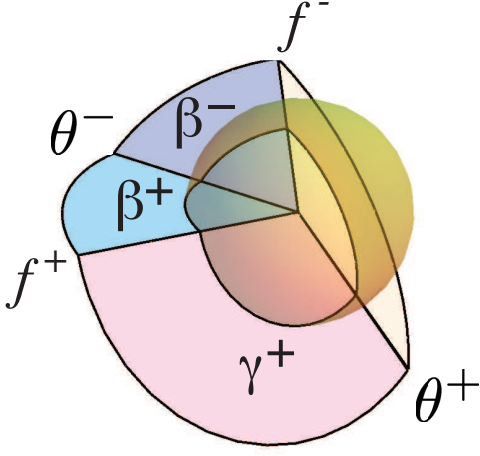


FIG. SI-1: Spherical polygons for a four-fold vertex. Angle variables are different from those used in the main text.

Supplementary Information

Appendix A: Vertex kinematics and spherical polygons

The intersection between an origami vertex and a sphere traces out a spherical polygon on the sphere surface [30] (Fig. SI-1). For a four-fold vertex, this polygon is a quadrilateral whose side lengths are inherited from the angles between adjacent folds in the fold pattern (the unlabeled fourth angle in Fig. SI-1 is $\gamma^- = 2\pi - \beta^+ - \beta^- - \gamma^+$). The relationship between dihedral angles f^\pm is

$$\begin{aligned} \cos \beta^+ \cos \gamma^+ + \sin \beta^+ \sin \gamma^+ \cos f^+ &= \\ \cos \beta^- \cos \gamma^- + \sin \beta^- \sin \gamma^- \cos f^- &. \end{aligned} \quad (\text{S1})$$

Since $\beta^+ + \gamma^+ = 2\pi - \beta^- - \gamma^-$, Eq. (S1) becomes

$$\sin \beta^+ \sin \gamma^+ (\cos f^+ + 1) = \sin \beta^- \sin \gamma^- (\cos f^- + 1) \quad (\text{S2})$$

A similar relationship between θ^+ and θ^- can be derived as

$$\sin \gamma^+ \sin \gamma^- (\cos \theta^+ + 1) = \sin \beta^+ \sin \beta^- (\cos \theta^- + 1) \quad (\text{S3})$$

The relationship between f^+ and θ^+ , however, is more complex (Fig. SI-2). Define ϵ to be the angle between θ^+ and θ^- given by

$$\cos \epsilon = \cos \beta^+ \cos \theta^+ + \sin \beta^+ \sin \theta^+ \cos f^+. \quad (\text{S4})$$

and such that $\epsilon = \beta^+ + \gamma^+$ when the vertex is flat. Then

$$\begin{aligned} \theta^+ &= \cos^{-1} \left(\frac{\cos \beta^+ - \cos \epsilon \cos \gamma^+}{\sin \epsilon \sin \gamma^+} \right) \\ &\pm \cos^{-1} \left(\frac{\cos \beta^- - \cos \epsilon \cos \gamma^-}{\sin \epsilon \sin \gamma^-} \right). \end{aligned} \quad (\text{S5})$$

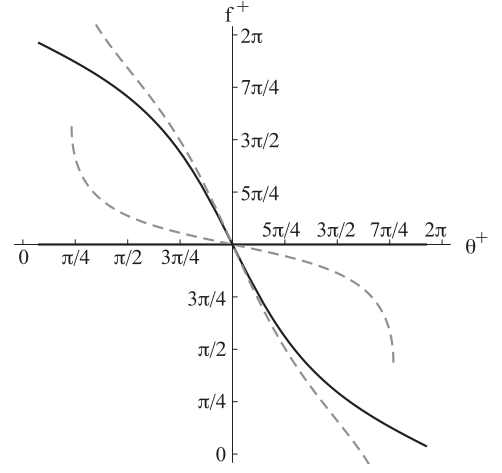


FIG. SI-2: The angle θ^+ versus f^+ for two cases: (solid) $\beta^+ = \beta^- = \pi/3$, $\gamma^+ = \gamma^- = 2\pi/3$ and (dashed) $\beta^+ = \pi/3 - \pi/10$, $\beta^- = \pi/3 + \pi/10$, $\gamma^+ = \gamma^- = 2\pi/3$. In each case, there are two distinct branches joined only at the flat state. Note that one of the branches for the solid curves lies along $f^+ = 0$.

Either sign in Eq. (S5) satisfies the geometric constraint equations; this ambiguity arises from the different branches of \cos^{-1} . Yet, the branches are physical, and correspond to different ways of choosing which folds are “mountain” and which folds are “valley” folds. In particular, there is a branch in which f^+ and f^- are both either mountain or valley folds and one in which they have the opposite sense [8]. In either case, however, $\cos f^\pm$ remains the same and the exponential solution for $u = 1 + \cos f$ in Eqs. 1 and 2 of the main text is valid.

One special case bears additional analysis. When the vertex has $\gamma^\pm + \beta^\pm = \pi$, the folds θ^+ and θ^- are collinear. In that case, one branch of the vertex has both f^+ and f^- as mountain (valley) folds. For the other branch, however, $f^+ = f^- = \pi$ is strictly satisfied and $\theta^+ = \theta^-$. That is simply the case that a vertex is folded along the line shared by θ^+ and θ^- , and this prevents the two adjacent folds f^\pm from folding at all. This motivates the choice of variables discussed in the main text, for which $\beta^\pm = \alpha \mp \beta$ and $\gamma^\pm = 2\pi - \alpha \mp \gamma$. Then $\beta = \gamma$ precisely when θ^\pm are collinear.

Appendix B: Second-order rigidity matrix for 1D strip

We label each unit cell with an index j and the two vertices within a unit cell with $n = 1, 2$. For convenience, we also express the dihedral angles in terms of their difference from π , $\delta f_n^\pm(j) = f_n^\pm(j) - \pi$ for the folds f^\pm of vertex n within unit cell j . Each vertex has one DOF, which we will parameterize with $\delta\theta_n^+(j)$. Since there is a two vertex unit cell, we combine these parameters into

two vectors,

$$\mathbf{f}(j) = \begin{pmatrix} f_1^-(j) \\ f_1^+(j) \\ f_2^-(j) \\ f_2^+(j) \end{pmatrix}, \quad (\text{S6})$$

and

$$\mathbf{s}(j) = \begin{pmatrix} \theta_1^+(j) \\ \theta_2^+(j) \end{pmatrix}. \quad (\text{S7})$$

Using spherical trigonometry, we compute $\mathbf{f}(j) = \mathbf{J}\mathbf{s}(j)$, where

$$\mathbf{J} = \begin{pmatrix} A_1^- + \sigma_1 B_1^- & 0 \\ A_1^+ + \sigma_1 B_1^+ & 0 \\ 0 & A_2^- + \sigma_2 B_2^- \\ 0 & A_2^+ + \sigma_2 B_2^+ \end{pmatrix}, \quad (\text{S8})$$

$\sigma_n = \pm 1$ is an arbitrary choice of branch in configuration space the vertex should be folded,

$$A_n^\pm = \frac{\sin(\alpha \mp \gamma_n)}{\sin(2\alpha)}, \quad (\text{S9})$$

and

$$B_n^\pm = \frac{1}{\sin(2\alpha)} \sqrt{\frac{\sin(\alpha - \gamma_n) \sin(\alpha + \gamma_n) \sin(\alpha \mp \beta_n)}{\sin(\alpha \pm \beta_n)}}. \quad (\text{S10})$$

For this paper, we have always assumed that $\sigma_n = 1$.

To complete our description, we must enforce the linear constraints $\delta f_1^-(j+1) - \delta f_2^+(j) = 0$ and $\delta f_2^-(j) - \delta f_1^+(j) = 0$. In Fourier space, these constraints lead to an equation of the form

$$\mathbf{R}(q)\mathbf{s}(q) = \mathbf{0}. \quad (\text{S11})$$

for the infinitesimal deformations of the origami strip, where

$$\mathbf{R}(q) = \begin{pmatrix} (A_1^- + B_1^-)e^{iq} & -(A_2^+ + B_2^+) \\ A_2^- + B_2^- & (A_1^+ + B_1^+) \end{pmatrix}. \quad (\text{S12})$$

Appendix C: Real-valuedness of the determinant: a hidden symmetry

We will restate the observed “reality” property here more formally. For all periodic triangulations we have checked, there exists a choice of unit cell so that the determinant of the rigidity matrix $\det \mathbf{R}(\vec{q})$ is real valued for all \vec{q} in the Brillouin zone. The consequence of this is that with such a choice of unit cell, the phase of $\det \mathbf{R}(\vec{q})$ cannot wind and so the topological polarization must vanish. There are also obvious consequences for the set of bulk zero modes which we will not discuss here. In Fig. SI-3 we display a sample calculation and visualization of this property for a small periodic triangulated origami, represented by a spring network.

This real-valuedness can be expressed in the following equivalent way. First, define $z_1 = e^{iq_1 a_1}$ and $z_2 = e^{iq_2 a_2}$,

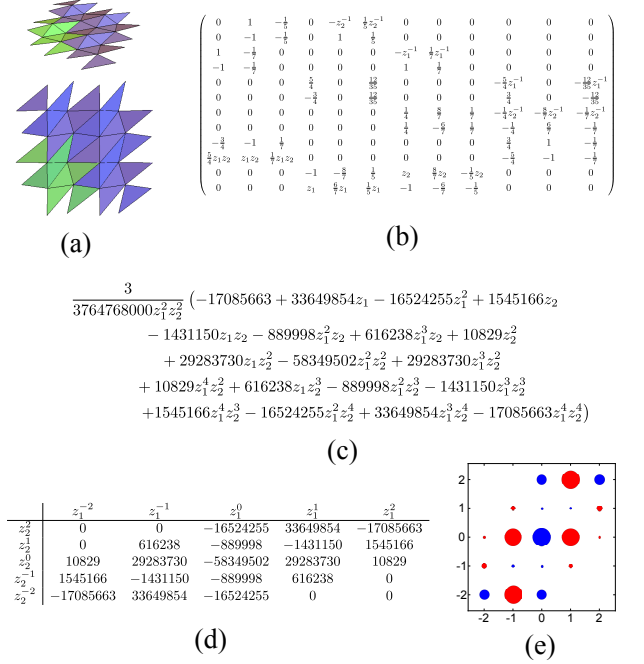


FIG. SI-3: Illustration of the reality property for triangulated origami. (a) A periodic triangulation based on the triangular lattice with four vertices, 12 edges and 8 triangles. The vertex coordinates are $(0, 0, 0)$, $(0, 1, 1/5)$, $(1, 1/7, 0)$, $(3/4, 1, -1/7)$ and the lattice primitive vectors are $(2, 0, 0)$ and $(0, 2, 0)$. Above is a side view and below is a top view. Four unit cells are shown, with one highlighted in green. (b) The Fourier transformed rigidity matrix $\mathbf{R}(z_1, z_2)$, where $z_1 = e^{iq_1 a_1}$ and $z_2 = e^{iq_2 a_2}$. Every row corresponds to an edge in the triangulation. (c) The Laurent polynomial $\det \mathbf{R}(z_1, z_2)$. (d) The table of coefficients of $\det \mathbf{R}(z_1, z_2)$, organized by powers of z_1 and z_2 . The number $3/3764768000$ has been factored out of all entries. (e) A graphical representation of the coefficients of $\det \mathbf{R}(z_1, z_2)$. Red dots are positive coefficients, blue dots are negative, and the area of the disks is proportional to the absolute value of the coefficients (with a minimum disk size imposed for visibility).

and observe that $\det \mathbf{R}(z_1, z_2)$ is a Laurent polynomial in those variables. Next, note that $\det \mathbf{R}(\vec{q})$ is real if and only if:

$$\begin{aligned} \det \mathbf{R}(\vec{q}) &= \overline{\det \mathbf{R}(\vec{q})} \\ \det \mathbf{R}(z_1, z_2) &= \overline{\det \mathbf{R}(z_1, z_2)} \\ &= \det \mathbf{R}(\bar{z}_1, \bar{z}_2) \\ &= \det \mathbf{R}(z_1^{-1}, \bar{z}_2^{-1}). \end{aligned}$$

In the third line, we use the fact that the coefficients of this polynomial are real, and in the final line, we use the fact that all \vec{q} in the Brillouin zone, z_1 and z_2 lie on the unit circle and so $\bar{z}_i = z_i^{-1}$. This shows that for all p, q , the coefficients of the $z_1^p z_2^q$ and $z_1^{-p} z_2^{-q}$ terms must be equal in order for this polynomial to be real-valued on the unit circle.

A change of unit cell merely changes $\det \mathbf{R}$ by a factor $z_1^m z_2^n$ where m and n are integers related to the change in the number of bonds crossing unit cell boundaries [11]. If one imagines the coefficients of $\det \mathbf{R}$ as a table (Fig. SI-3(d)), then such a factor does not change the values in the table, but merely shifts the positions of the entries in the table by a vector (m, n) . Therefore, the “reality property” is equivalent to the polynomial $\det \mathbf{R}(z_1, z_2)$ being “2D palindromic”, i.e.

$$\det \mathbf{R}(z_1^{-1}, z_2^{-1}) = z_1^k z_2^l \det \mathbf{R}(z_1^{-1}, z_2^{-1}), \quad (\text{S13})$$

for some integers k, l . Equivalently, the table of coefficients of $\det \mathbf{R}(z_1, z_2)$ is symmetric under inversion through some point $(k/2, l/2)$.

Examples and tests performed: We generated small triangulations of a torus via flipping edges from the triangular lattice and in all cases checked found that the the polynomial $\det \mathbf{R}(z_1, z_2)$ was a palindrome. To ensure that loss of precision from floating-point operations were not an issue, we did these computations in rational arithmetic in the Mathematica computer algebra system.

Specifically, we began with periodic triangulation “seeds” displayed in Fig. SI-4 and performed random edge flips (transforming two adjacent triangles into two different triangles on the same four vertices) repeatedly onto randomly chosen edges. This procedure is illustrated in Fig. SI-4(a).

For every such crease pattern generated, we used vertex coordinates made by randomly perturbing a flat embedding of the seed triangulation. These were rounded to the nearest rational number with denominator lower than 10. The Laurent polynomial $\det \mathbf{R}(z_1, z_2)$ was then calculated exactly and the coefficients of different terms were compared to check whether the polynomial was indeed palindromic as in Eq. (S13). In some cases, a flip would cause this polynomial to vanish (due e.g. to a degenerate edge connecting a vertex to itself). Afterwards, it is quite likely that further flips would produce triangulations with zero determinant. While the zero polynomial is of course real-valued, in order to get more interesting tests, if this occurred, we rejected this triangulation and flipped another edge instead. Regardless, for all triangulated origami checked we found that Eq. (S13) was always satisfied. In Table I we show a summary of the tests performed.

Partial result: We can show that subdividing a triangle in triangulated origami preserves the property that $\det \mathbf{R}(\vec{q})$ remains real. To see this, note that such a subdivision creates one new vertex and three edges. With an appropriate choice of unit cell we can ensure that this vertex is not on the boundary and thus does not pick up factors of $e^{iq_1 a_1}$ or $e^{iq_2 a_2}$.

The new vertex introduces three columns into $\mathbf{R}(\vec{q})$ whose only nonzero entries can be in the rows corresponding to the three new edges. By reordering the vertices and columns, one finds that the determinant takes a block upper-triangular form with a 3×3 block on the diagonal from the new additions (which we call $\mathbf{R}_n(\vec{q})$)

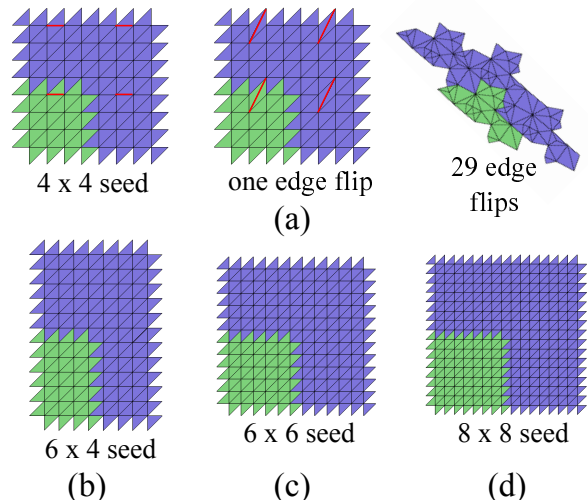


FIG. SI-4: Seed triangulations and edge flips. In each image, four unit cells are shown, with one highlighted in green. The triangulations are only shown with planar embeddings for clarity, the actual tested triangulations were deformed into three dimensions. (a) left: The 4 by 4 seed triangulation with one highlighted edge, center: the triangulation resulting from the edge flip of the red edge, right: a triangulation resulting from 29 random edge flips on the seed. (b) The 6 by 4 seed triangulation. (c) The 6 by 6 seed triangulation. (d) The 8 by 8 seed triangulation.

seed	$ V $	$ E $	$ T $	(runs, flips)
4 by 4	16	48	32	(100, 1000)
6 by 4	24	72	48	(50, 500)
6 by 6	36	108	72	(20, 200)
8 by 8	64	192	128	(10, 100)

TABLE I: Summary of tests performed of the “reality” property on different families of periodic triangulated origami. Each line of the table corresponds to a different seed (depicted in Fig. SI-4), and displays the number of vertices $|V|$, edges $|E|$ and triangles $|T|$ in the seed and shows the number of runs started as well as the number of random flip operations performed. Note that a flip preserves $|V|$, $|E|$ and $|T|$, and that the computations require computing determinants of symbolic $|E| \times 3|V|$ matrices. In all runs, every single triangulation generated had the reality property, as described in the text.

as well as $\mathbf{R}_0(\vec{q})$ as another block on the diagonal. By a well-known property of the determinant, this implies that $\det \mathbf{R}(\vec{q}) = \det \mathbf{R}_n(\vec{q}) \det \mathbf{R}_0(\vec{q})$.

If we were able to prove an analogous result for edge flips, then we would have shown that the palindromic property holds for all triangulations.

Appendix D: On the design of topological kirigami

We found topologically polarized kirigami via the following steps. We first constructed the pattern of plates and hinges as follows. As in Appendix C, we began with

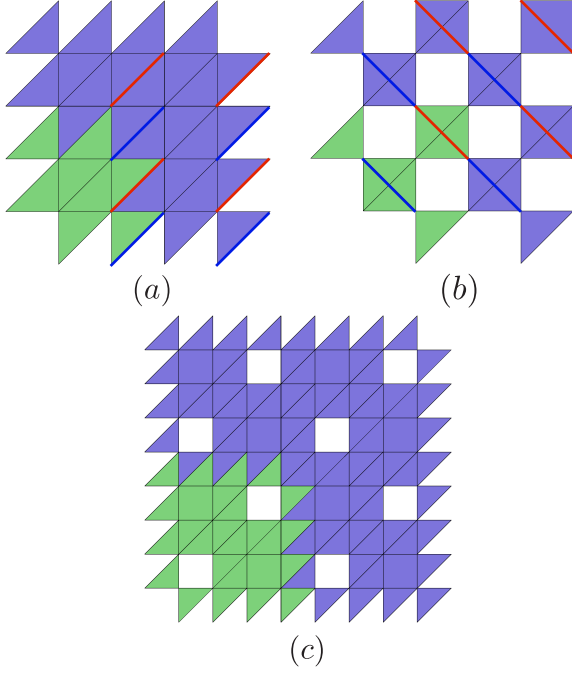


FIG. SI-5: Schematics of some structures created while designing the kirigami. In each image, four unit cells are shown, with one highlighted in green. These images only show the pattern of hinges and plates, and do not represent 3D embeddings. (a) A triangulated origami based on the triangular lattice. Two families of creases are highlighted in red and blue which are moved to create the next structure. (b) The checkerboard lattice of tetrahedra. This structure consists of tetrahedra joined by universal joints at their vertices. (c) The final kirigami structure. Created by placing rows and columns of additional triangles between tetrahedra, and then replacing the tetrahedra with flat quadrilateral plates.

a periodic spring network with the combinatorics of the standard triangular lattice (drawn in Fig. SI-5(a) as a square lattice with all NE diagonals added). This pattern models a triangulated origami structure, which seems to have a real determinant. To try to break this symmetry we attempted to add holes in the unit cell.

To add holes without changing the marginal rigidity property, we removed one NE diagonal bond from a square A and placed it in an adjacent (already occupied) square B as a NW diagonal bond. This yields a hole in A and a new tetrahedron in B . If one does this for all squares in a checkerboard pattern, one ends up with the so-called checkerboard lattice of tetrahedra (Fig. SI-5(b)). This is the simplest 2D periodic structure in 3D which admits geometric realizations with distinct topological polarizations. However, the tetrahedra are joined at vertices, not along hinges, so it is neither origami nor kirigami.

To remedy this, we may add rows and columns of triangulated strips between the holes and the tetrahedra. Now we do have a structure made of solid bodies joined along

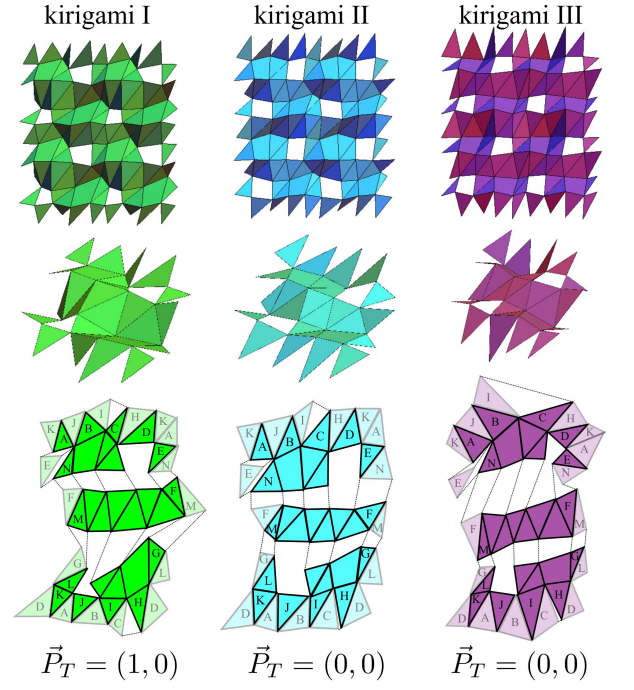


FIG. SI-6: Three kirigami unit cells with different topological polarizations. A top view and side view of the 3D unit cells are shown above exploded versions that have been cut into strips and then flattened into the plane. The dashed lines indicate how the strips are to be joined to create the 3D structure shown above and the faces labeled by letters indicate the periodicity of the structure.

hinges, but the bodies are tetrahedra and not yet flat plates. Flat plates can be modeled by a spring network with pyramids. By adding an additional vertex above the plate and attaching it to the four vertices of the we create a minimally rigid body which is attached to the structure by four coplanar hinges. The final pattern of hinges and plates is shown in Fig. SI-5(c) (pyramids not shown for clarity).

Given this design, we still have to find a suitable realization of this structure as a 3D object. We did this by beginning with a flat embedding of a unit cell and perturbing the vertices randomly, subject to the condition that the quadrilateral plates remain planar. These randomly generated unit cells were then checked to determine if they had a topological polarization. Fig. SI-6 shows the unit cells of three kirigami structures with this crease pattern but with differing topological polarizations: kirigami I has polarization $(1, 0)$, and kirigami II and III have polarization $(0, 0)$. Their 3D structures are also displayed in an “exploded” view, where they have been cut apart into flattened strips which must be bent in space and then glued together to form the kirigami structures. Unit cells I and II were used to construct the domain wall in Fig. 3 in the main text.

In Fig. SI-7 we show kirigami structures consisting of pairs of unit cells from Fig. SI-6. The domain walls do

not contain any extra or missing bonds, so there are no differences in the local counting of degrees of freedom. These kirigami structures are rectangular sheets with periodic boundary conditions in both directions, so one might expect the lowest energy vibrational modes to be bulk bending modes. This is indeed the case when the two unit cells used have the same polarization vector (Fig. SI-7(a)). However, when a structure is made

of unit cells with two distinct polarizations, one of the domain walls carries localized very low-energy modes (Fig. SI-7(b) and Fig. 3 in the main text). The eigenvalue corresponding to the energy of the topological mode is $\omega^2 = 1.42 \times 10^{-16}$ (comparable to the eigenvalues corresponding to the translational zero modes), whereas the eigenvalue corresponding to the bending mode is much larger, $\omega^2 = 1.82 \times 10^{-9}$.

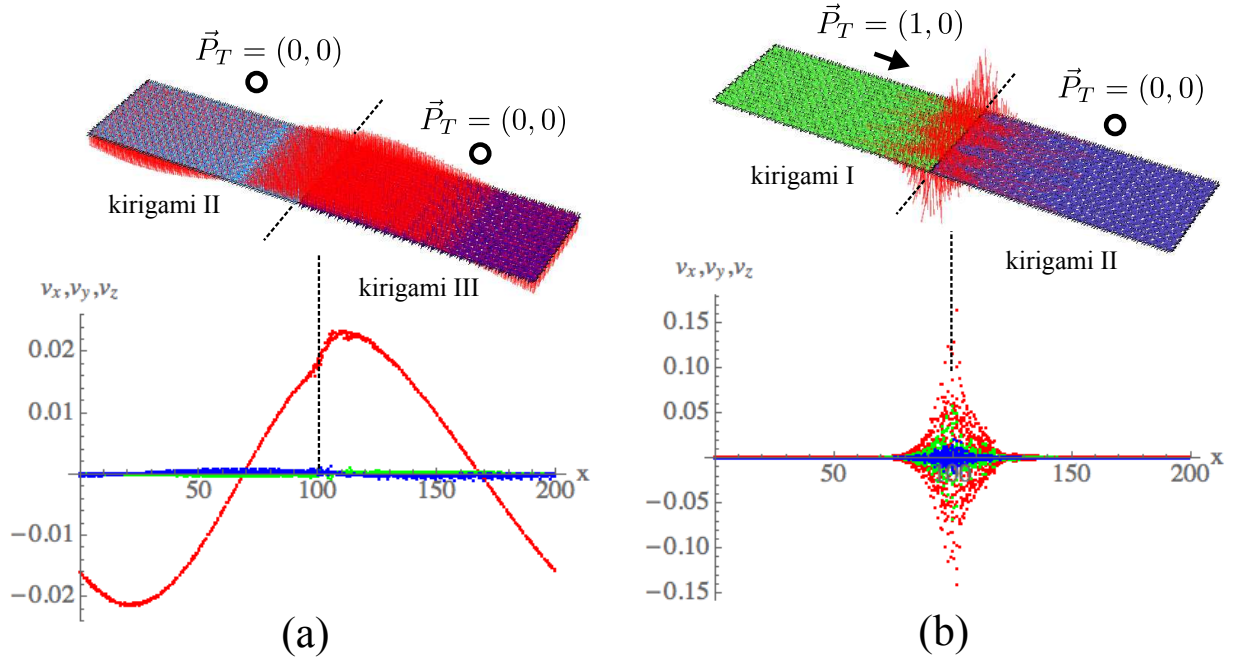


FIG. SI-7: Composite kirigami systems constructed from unit cells I, II and III from Fig. SI-6 and their lowest energy eigenmodes. Both structures depicted consist of 50 unit cells (along the x -direction) by 5 unit cells (along the y -direction), which are divided into two domains each of size 25 by 5. Two copies in the shorter direction are shown in the upper figures, and the displacements in the mode are overlaid as red lines. The structures are periodic in both directions, so there are domain walls at $x = 0 = 200$ and $x = 100$. The domain wall at $x = 100$ is marked with dashed lines. The lower plots show the x -, y - and z -components (in blue, green, and red, respectively) of the displacement vectors of all vertices as a function of the x -positions. (a) Composite structure of kirigami II and III, both of which have polarization $(0,0)$. The lowest eigenmode has eigenvalue $\omega^2 = 1.82 \times 10^{-9}$ and resembles a bulk bending mode. (b) Composite structure of kirigami I (polarization $(1,0)$) and II (polarization $(0,0)$). The lowest eigenmode has eigenvalue $\omega^2 = 1.42 \times 10^{-16}$ and is highly localized near the domain wall at $x = 100$.